Prediction of the low-velocity distribution from the pore structure in simple porous media

Pietro de Anna, Bryan Quaife, George Biros, and Ruben Juanes

Phys. Rev. Fluids **2**, 124103 — Published 22 December 2017

DOI: 10.1103/PhysRevFluids.2.124103

Prediction of low velocity distribution from pore structure in simple porous media

Pietro de Anna,[1,*] Bryan Quaife,[2,†] George Biros,[3,‡] and Ruben Juanes[4,§]

[1] Institut des sciences de la Terre, University of Lausanne, Lausanne 1015, Switzerland
[2] Department of Scientific Computing, Florida State University, 400 Dirac Science Library, Tallahassee, Florida 32306, USA
[3] Institute for Computational Engineering and Sciences, The University of Texas at Austin, 201 East 24th St, Austin, Texas 78712, USA
[4] Massachusetts Institute of Technology, 77 Massachusetts Ave, Building 1, Cambridge, Massachusetts 02139, USA

The macroscopic properties of fluid flow and transport through porous media are a direct consequence of the underlying pore structure. However, precise relations that characterize flow and transport from the statistics of pore-scale disorder have remained elusive. Here, we investigate the relationship between pore structure and the resulting fluid flow and asymptotic transport behavior in 2D geometries of non overlapping circular posts. We derive an analytical relationship between the pore throat size distribution $f_\lambda \sim \lambda^{-\beta}$ and the distribution of the low fluid velocities $f_u \sim u^{-\beta/2}$, based on a conceptual model of *porelets* (the flow established within each pore throat, here a Hagen–Poiseuille). Our model allows us to make predictions—within a Continuous Time Random Walk (CTRW) framework—for the asymptotic statistics of spreading of fluid particles along their own trajectories. These predictions are confirmed by high fidelity simulations of Stokes flow and advective transport. The proposed framework can be extended to other configurations which can be represented as a collection of known flow distributions.

PACS numbers: 47.56.+r, 92.40.Kf, 05.60.Cd, 05.40.Fb

I. INTRODUCTION

In soil, aquifers, industrial filtration systems and may other situations, the motion of fluids is confined within small spaces, typically of size λ ranging between 10^{-6} – 10^{-2} m. In this conditions, fluids flowing through such confined media are forced to pass between solid impermeable obstacles (grains, represented by gray disks in fig. 1) that separates spaces (pores) that can be filled by the flow: the associated velocities of fluids are typically very small, on the order of $u \sim 1 - 100\,\mu\text{m/s}$ ($\sim 0.1 - 10\,\text{m/d}$) [1]. These porous media flows have a rich structure whose spatial and temporal complexity plays a critical role in natural and engineered processes such as groundwater contamination and remediation [2, 3], water infiltration in soil [4], geologic carbon sequestration [5], enhanced hydrocarbon recovery [6], water filtration systems [7] and polymer electrolyte fuel cells [8]. Traditionally, the heterogeneity of these flows is considered at scales where the main structure of the host medium varies, e.g. varying from one type of rock to another in a geological formation, but the organization of grains and pores, is not resolved. In these situations, the fluid motion is represented by an averaged, Darcy-like, flow through an equivalent continuous permeability field, that represents the ability of the host medium to transmit the fluid, as a result of an applied pressure gradient [9].

* pietro.deanna@unil.ch
† bquaife@fsu.edu
‡ gbiros@acm.org
§ juanes@mit.edu

Due to the complex geometry of the connected pore space, it has been challenging to formulate predictive models for permeability based on the knowledge of the main medium features. Semi-empirical relations between medium structure, such as porosity or grains size, and permeability [10, 11] have been validated and extended for specific media [12–14]. However, the theoretical determination of fluid velocity distributions, which characterize its heterogeneity, from statistical descriptions of pore-scale geometry remains an open challenge. Understanding and quantifying velocity heterogeneity in porous media is important because it controls the late times particle spreading [15–20] and fluid mixing [21–24], which also mediates chemical reactions [25–29] and biological activities [30, 31].

Laboratory experiments on bead packs [1, 32–36], sand columns [37] and real rock samples [38, 39], as well as numerical simulations at the pore scale [19, 32, 33, 40–43] have shown the emergence of highly heterogeneous velocity distributions, even in simple macroscopically homogeneous porous media. This velocity heterogeneity leads to consequences at larger scale that can be quantified in terms of anomalous particle-transport behavior such as early arrival and late-time tailing of breakthrough curves, non-Gaussian plume shape and nonlinear scaling of mean square displacement (MSD). These phenomena can be captured and understood only after direct observation or computational characterization of the pore-scale fluid mechanics [41].

Earlier experimental [35, 36, 39] and computational [19, 40, 41, 44, 45] studies have identified distinct behaviors for high and low velocities. High velocities are controlled by the formation of channels, while low velocities

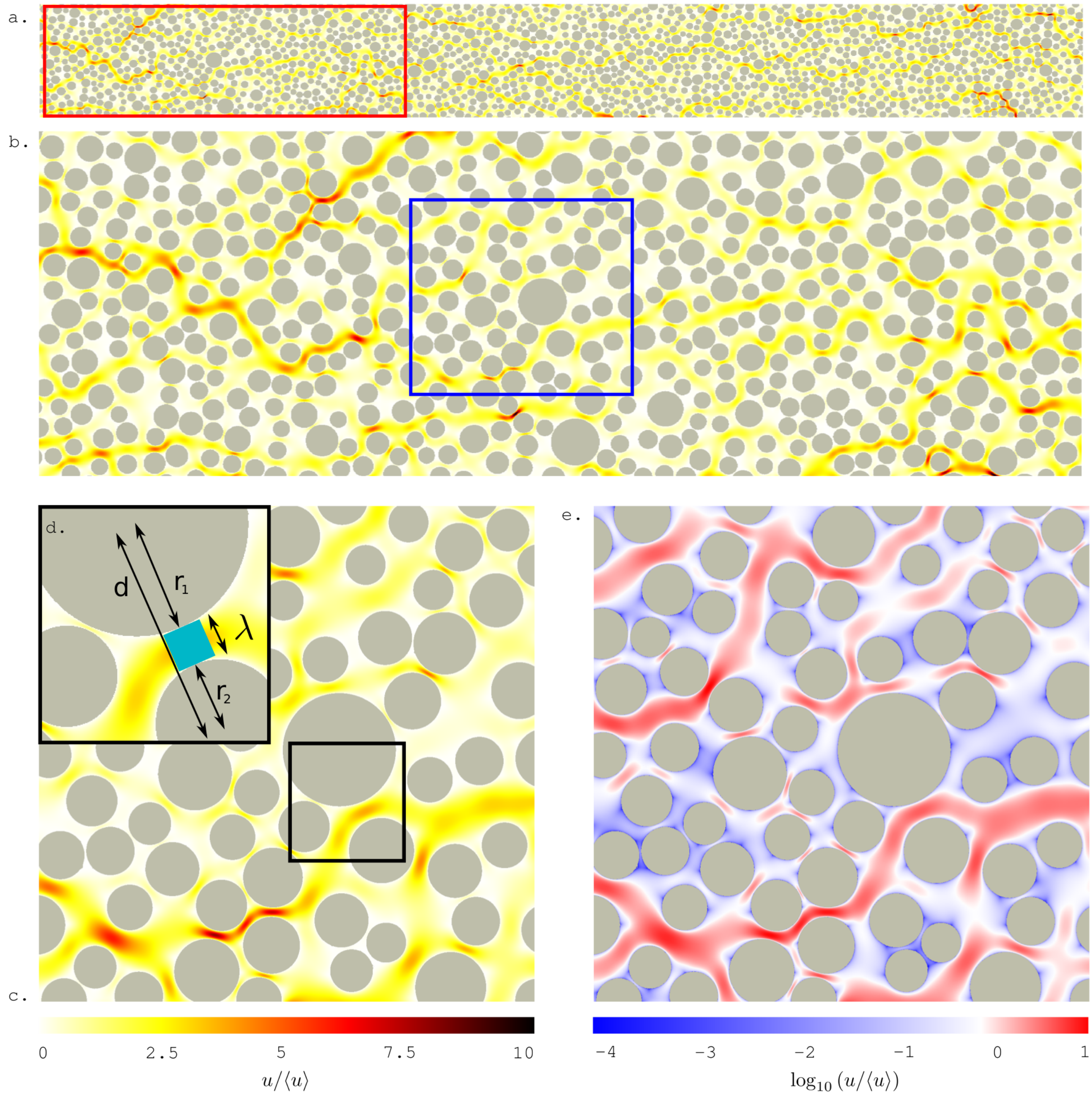

FIG. 1. a. Representation of the 2D porous media considered in this study, showing the disordered arrangement of disks (gray circles), and the magnitude of the fluid velocity from a high fidelity simulation of Stokes flow rescaled by the mean velocity, $u/\langle u\rangle$. b. Zoomed-in view of the red box in a. c. Zoomed-in view of the blue box in b. d. Schematic of the conceptual model of pipes (cyan squares) associated with pore throats. e. Same field as in c, in logarithmic scale. Red color indicates an above-average velocity; blue color indicates a below-average velocity.

are dominated by stagnation zones. Recent studies have proposed phenomenological models for the distribution of high velocities—including stretched exponential [46] and power-exponential [45] distributions—but without an underlying mechanistic or statistical physics theory.

The macroscopic transport through porous media has been extensively studied by tracking the displacement of fluid particles along their trajectories (e.g. [47]). While the high velocities control the overall ability of the medium to transmit the fluid, the distribution of low velocities in zones of fluid stagnation have been shown to control and characterize late-time asymptotic particle transport statistics [19, 41], mixing [22], and reactive transport [28]. To provide a conceptual explanation of this phenomenon, one may consider the evolution of a plume of a passive tracer in a heterogeneous medium. Plume spreading in the flow direction is determined by two simple mechanisms: fast migration of the leading part of the plume along high-velocity channels, and trapping of the trailing part of the plume in stagnation zones. This contrast in velocities, quantified by the broadness of the velocity distribution, controls the spreading rate of the plume. It has been shown theoretically [e.g., 15] and numerically [e.g., 48, 49], and has been confirmed in field and laboratory experiments [e.g., 29, 50], that the described mechanisms of advective spreading are persistent and dominate transport and mixing for times much longer than the characteristic diffusive time over scale of heterogeneity of the medium. Therefore, the possibility to estimate the flow heterogeneity—in particular, the distribution of low velocities that are known to control asymptotic transport properties [15, 44, 47, 51]—based on knowledge of the host medium structure alone would constitute a powerful tool.

To understand the origin of asymptotic transport behavior, we investigate the relationship between the structure of the host medium and the resulting distribution of fluid velocities in stagnation zones. We consider 2D porous media whose solid, impermeable structure consists of non overlapping circular disks of random position and radius (Fig. 1). This disordered arrangement of disks can be characterized geometrically by constructing a Delaunay triangulation of the disk centers [e.g., 52]: each triangle defines a *pore body* and each edge defines a *pore throat* (Fig. 2a). We characterize the statistical properties of the medium through the distribution of pore throat size, $\lambda = d - r_1 - r_2$, where d is the distance between the two disk centers connected by an edge of the Delaunay triangulation, and r_1, r_2 are the respective disk radii (Fig. 1d). The random position and size of the disks are generated such that the probability density function (PDF) of pore throat size is a power law $f_\lambda(\lambda) \sim \lambda^{-\beta}$, with $\beta > 0$. We generate five pore geometries whose distribution is power-law for small pores ($0.01 < \lambda/\langle\lambda\rangle < 0.2$) and it has a cut-off for large pores. The range of pore sizes distributed as a power law are characterized by the exponent β which, for the 5 geometries considered, takes the value $\beta = 0.25, 0.22, 0.17, 0.12, 0.08$. The geometry associated with $\beta = 0.17$ is illustrated in Fig. 1 (see Fig. 7 for all five geometries).

Pore network models have been used in the past to study flow and flow-driven processes in complex pore structures. These models are based on the knowledge of some properties of the geometry of the pore space. Therefore, the pore networks are often constructed directly from images of porous media obtained with small scale imaging techniques [40], like X-ray micro-tomography, and the associated models are made by assuming hypothesis about what is a pore and what is a throat and how they are connected [53]. To the best of our knowledge, no pore network model or other type of analysis have been used, to date, to successfully investigate low velocities, in the range $10 - 10^4$ times smaller than the average one. To this end we use a high-resolution numerical method described in Section II, allowing to accurately quantify the distribution of such low velocities.

Our aim is to derive an analytical relationship between the pore throats size distribution (the smallest openings constraining the fluid flow) and the fluid velocity probability density function (PDF). To do that, we hypothesize that what controls this relationship is the distribution of the throats size and not the connectivity between pores (which probably control the permeability and, thus, the overall flow), which we neglect. Strictly, large pores also contain a fraction of small velocities. However, because small pores are much more abundant (pore throats are power law distributed), we argue that it is reasonable to assume that the distribution of small velocities is controlled by the distribution of small openings.

II. METHODS

We simulate steady incompressible flow through each pore geometry, driven by a pressure gradient from left to right, and with no-flow boundary conditions at the top and bottom boundaries. We simulate flows at low Reynolds numbers, $\mathrm{Re} = \frac{\rho\,\langle\lambda\rangle\,\langle u\rangle}{\mu} < 10^{-2}$, where $\langle\lambda\rangle$ is the mean pore throat size, $\langle u\rangle$ is the mean velocity magnitude, ρ is the fluid density, and μ is the fluid dynamic viscosity. Under these conditions, the flow is Stokesian, and is described by the equations:

$$\mu\nabla^2\boldsymbol{u} = \nabla p, \quad \nabla\cdot\boldsymbol{u} = 0, \tag{1}$$

where p is the fluid pressure and $\boldsymbol{u}$ is the fluid velocity. We neglect the gravitational term since we assume that the flow is horizontal, and we impose no-slip boundary conditions at the boundary of each disk.

The Stokes equations are recast in terms of a vector-valued density function $\boldsymbol{\sigma}$ by using the indirect integral equation [54]

$$\boldsymbol{u}(\boldsymbol{x}) = \frac{1}{\pi}\int_\Gamma \frac{\boldsymbol{r}\cdot\boldsymbol{n}}{\|\boldsymbol{r}\|^2}\frac{\boldsymbol{r}\otimes\boldsymbol{r}}{\|\boldsymbol{r}\|^2}\boldsymbol{\sigma}(\boldsymbol{y})ds_{\boldsymbol{y}}, \quad \boldsymbol{x}\in\Omega, \tag{2}$$

where $\boldsymbol{r} = \boldsymbol{x} - \boldsymbol{y}$, Γ is the boundary of the geometry Ω, and $\boldsymbol{n}$ is unit outward normal of Γ at $\boldsymbol{y}$. Eq. (2) is called the double-layer potential and can be expressed in component form as

$$u_1(\boldsymbol{x}) = \frac{1}{\pi}\int_\Gamma \frac{\boldsymbol{r}\cdot\boldsymbol{n}}{\|\boldsymbol{r}\|^2}\frac{\boldsymbol{r}\cdot\boldsymbol{\sigma}}{\|\boldsymbol{r}\|^2}r_1(\boldsymbol{y})ds_{\boldsymbol{y}},$$

$$u_2(\boldsymbol{x}) = \frac{1}{\pi}\int_\Gamma \frac{\boldsymbol{r}\cdot\boldsymbol{n}}{\|\boldsymbol{r}\|^2}\frac{\boldsymbol{r}\cdot\boldsymbol{\sigma}}{\|\boldsymbol{r}\|^2}r_2(\boldsymbol{y})ds_{\boldsymbol{y}},$$

where $\boldsymbol{r} = (r_1, r_2)$. In addition, the pressure can be computed by evaluating the integral

$$p(\boldsymbol{x}) = -\frac{\mu}{\pi} \int_\Gamma \frac{1}{\|\boldsymbol{r}\|^2} \left(I - 2\frac{\boldsymbol{r} \otimes \boldsymbol{r}}{\|\boldsymbol{r}\|^2} \right) \boldsymbol{n} \cdot \boldsymbol{\sigma}(\boldsymbol{y}) ds_{\boldsymbol{y}}, \quad (3)$$

where I is the 2×2 identity matrix.

To avoid the two-dimensional Stokes paradox, we bound the disks by a rounded-off rectangular boundary Γ_0. We use a Dirichlet boundary condition on Γ_0 to prescribe a plug flow at the left and right ends of the channel and a no-slip condition at the top and bottom of the channel (Fig. 1a). Letting $\boldsymbol{f}$ be the above described Dirichlet boundary condition, the density function $\boldsymbol{\sigma}$ must satisfy the second-kind Fredholm integral equation [54]

$$\boldsymbol{f}(\boldsymbol{x}) = -\frac{1}{2}\boldsymbol{\sigma}(\boldsymbol{x}) + \frac{1}{\pi} \int_\Gamma \frac{\boldsymbol{r} \cdot \boldsymbol{n}}{\|\boldsymbol{r}\|^2} \frac{\boldsymbol{r} \otimes \boldsymbol{r}}{\|\boldsymbol{r}\|^2} \boldsymbol{\sigma}(\boldsymbol{y}) ds_{\boldsymbol{y}}, \quad \boldsymbol{x} \in \Gamma. \quad (4)$$

To summarize, solving Eq. (1) using an indirect integral equation formulation requires a two-step procedure. First, Eq. (4) must be solved for the density function $\boldsymbol{\sigma}$. Second, the velocity $\boldsymbol{u}(\boldsymbol{x})$ is computed for any $\boldsymbol{x} \in \Omega$ using Eq. (2). In addition, if required, the pressure can be computed using Eq. (3). Therefore, the accuracy of the method is completely determined by two approximations. First, the accuracy of $\boldsymbol{\sigma}$, which depends on the quadrature method used to approximate the integral in Eq. (4), and, second, the quadrature method used to approximate the integral in Eq. (2) and Eq. (3).

To approximate the density function $\boldsymbol{\sigma}$, Eq. (4) is discretized at a set of collocation points $\{\boldsymbol{x}_j\}_{j=1}^N$ and the integral is replaced with the trapezoid rule. The result is the dense linear system

$$\boldsymbol{f}_j = -\frac{1}{2}\boldsymbol{\sigma}_j + \sum_{k=1}^N K(\boldsymbol{x}_j, \boldsymbol{x}_k) \Delta s_k \boldsymbol{\sigma}_k, \quad j = 1, \dots N \quad (5)$$

where Δs_j is the Jacobian of Γ at $\boldsymbol{x}_j$,

$$\boldsymbol{f}_j = \boldsymbol{f}(\boldsymbol{x}_j), \quad \boldsymbol{\sigma}_j = \sigma(\boldsymbol{x}_j), \quad \text{and}$$
$$K(\boldsymbol{x}, \boldsymbol{y}) = \frac{1}{\pi} \frac{\boldsymbol{r} \cdot \boldsymbol{n}}{\|\boldsymbol{r}\|^2} \frac{\boldsymbol{r} \otimes \boldsymbol{r}}{\|\boldsymbol{r}\|^2}.$$

The diagonal term $K(\boldsymbol{x}_j, \boldsymbol{x}_j)$ is replaced with the limiting value

$$\lim_{\substack{\boldsymbol{y} \to \boldsymbol{x} \\ \boldsymbol{y} \in \Gamma}} K(\boldsymbol{x}, \boldsymbol{y}) = \frac{\kappa(\boldsymbol{x})}{2\pi} (\mathbf{t}(\boldsymbol{x}) \otimes \mathbf{t}(\boldsymbol{x})), \quad \boldsymbol{x} \in \Gamma,$$

where $\kappa(\boldsymbol{x})$ is the curvature at $\boldsymbol{x}$, and $\mathbf{t}(\boldsymbol{x})$ is the unit tangent vector at $\boldsymbol{x}$. Since the trapezoid rule has spectral accuracy for smooth periodic functions [55], the solution of Eq. (5) converges with spectral accuracy to the exact solution of Eq. (4).

Eq. (5) is solved iteratively with GMRES [56] which requires a mesh-independent number of iterations [57]. To accelerate the numerical solver, the necessary matrix-vector multiplication is done in linear time with the fast multipole method [58]. Finally, the number of GMRES iterations is reduced by applying a block-diagonal preconditioner, where each block corresponds to an individual disk.

Once $\boldsymbol{\sigma}_j$ is computed with spectral accuracy, the velocity $\boldsymbol{u}(\boldsymbol{x})$ for $\boldsymbol{x} \in \Omega$ can be approximated. This is done by replacing the integral in Eq. (2) with the trapezoid rule with the same quadrature nodes used to solve Eq. (4)

$$\boldsymbol{u}(\boldsymbol{x}) \approx \sum_{k=1}^N K(\boldsymbol{x}, \boldsymbol{x}_k) \sigma_k \Delta s_k, \quad \boldsymbol{x} \in \Omega.$$

The velocity is computed on a regular set of Eulerian points in Ω. When $\boldsymbol{x}$ is close to one of the disks, the accuracy of the trapezoid rule deteriorates since the integrand becomes nearly singular, and a near-singular integration strategy must be used. We adopt the strategy described in [59] which achieves fifth-order accuracy with only a slight increase in the algorithmic complexity. At the resolution we use, the smallest resolved velocity is approximately $u_{\max}/10^5$, where $u_{\max}$ is the value of the maximum velocity simulated.

III. RESULTS

A simulated velocity field is shown in Fig. 1 for one of the geometries studied, corresponding to the pore throat size distribution power-law exponent $\beta = 0.22$. It is apparent that, despite the simplicity of the porous medium, the velocity develops a complex spatial structure that combines high-velocity channels with low-velocity stagnation zones (Fig. 1e), which have been shown to play a major role in determining the fluid longitudinal and transverse asymptotic dispersion of transported particles [19, 41].

We study the distribution of the velocity magnitudes $u = \|\boldsymbol{u}\|$, and its dependence on the characteristics of the porous medium. The medium geometry is characterized by the exponent β of the power law in the low range of pore throat size, $f_\lambda \sim \lambda^{-\beta}$. To characterize the velocity, we define the rescaled velocity magnitude, $u_r = u/\langle u \rangle$. We find that the low velocities are well fitted by a power law with an exponent that depends on the pore throat size distribution, $f_{u_r} \sim u_r^{-\beta/2}$ for $u_r \ll u_{\max}$ (Fig. 4a,b). High velocities, in contrast, are well described by an exponential function, and the exponent of the distribution does not exhibit a detectable dependence on the pore geometry statistics (Fig. 4c). To ensure that our numerical method is accurate enough to capture the low velocities distribution, for one geometry, we generated the same velocity field on a finer grid and found that the velocity distribution is unchanged. Therefore, the spatial resolution of the numerical scheme is sufficiently fine to resolve the smallest pore throat generated, and obtains a velocity distribution that is independent of the computational grid.

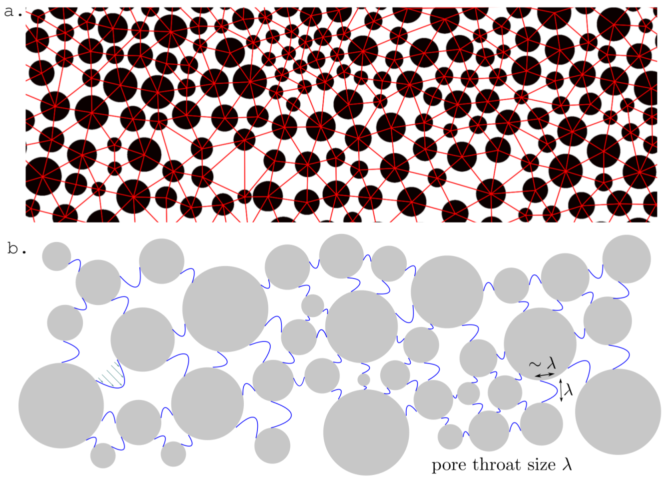

FIG. 2. a. Detail of the Delaunay triangulation of the pore geometry: edges of the triangulation connecting the centers of neighboring disks (red segments) define the pore throats. b. Proposed conceptual model of *porelets*, consisting of a collection of pore flows along pore throats (each of given width λ and length $c\lambda \sim \lambda$): for this simple geometry each porelet is a Hagen–Poiseuille parabolic profile.

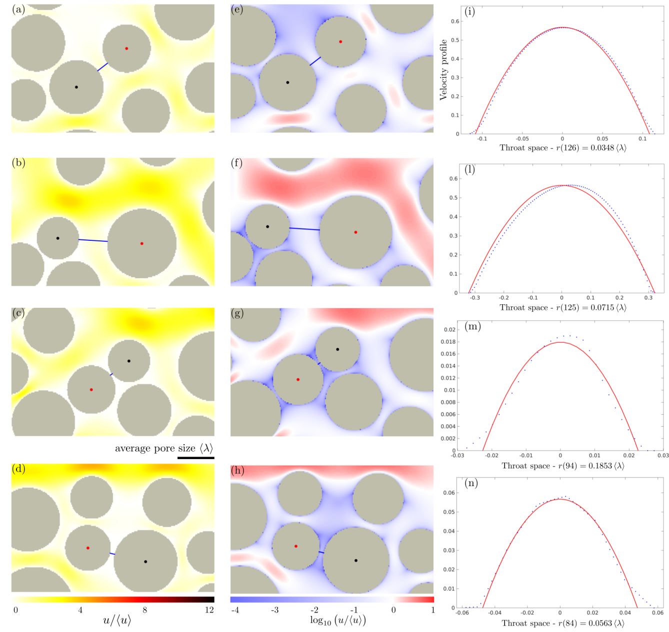

FIG. 3. Zoomed-in views of the magnitude of the velocity field around 4 typical pore throats with colormap in natural scale (left column) and logarithmic scale (center column), and the its interpolation along the segment connecting the grain walls (right column). A parabolic fit (red solid line) is superposed to the interpolation data (blue symbols).

TABLE I. Mean normalized residual $\langle r_u \rangle$ of the parabolic fit to the velocity profile along pore throats, for the five flow configurations considered in our study.

β	n_{disks}	n_{throats}	$\langle r_u \rangle$
0.25	1660	1912	0.057
0.22	893	1182	0.055
0.17	823	962	0.053
0.12	753	931	0.047
0.08	994	1074	0.063

We develop a novel model, based on a statistical approach, to explain the observed distribution of the low velocities. In analogy with pore network models [e.g., 60–66], we understand the overall flow as equivalent to one through a collection of flow in pores, the porelets, that for these geometries result in Hagen–Poiseuille flows through pipes of distributed size. In contrast with network models, however, here we are interested in reproducing the low velocity behavior in the pore space, that is, velocities in the range 10 to 10^4 times *smaller* than the mean Eulerian velocity. Please note that we can investigate such a wide range of velocities due to the powerful and recent numerical scheme that we have adopted.

The velocities through the porous medium are locally controlled by the size of the smallest openings, the pore throats, therefore, we conceptualize the flow through each throat of size λ, a porelet, as the one through a pipe, of width λ and length l which we assume begin proportional to it $l = c\lambda$ (Fig. 2b), driven by a single effective pressure gradient $\langle \nabla_{||} p \rangle$ along the pipe itself. This simple conceptual model neglects the pore connectivity and is consistent with the isotropy of a porous material (in contrast with a fractured medium, where the fracture orientation determines a preferential direction). Moreover, it is supported by the direct observation of the parabolic velocity profile within throats [1, 32, 40]. The fluid velocity through a pipe has only longitudinal component [67], and its magnitude has a parabolic profile:

$$u(y) = \frac{-\langle \nabla_{||} p \rangle}{2\mu} \left[\left(\frac{\lambda}{2} \right)^2 - y^2 \right].$$

Letting $A = \frac{-\langle \nabla_{||} p \rangle}{2\mu}$, the maximum velocity, achieved at the pipe centerline ($y = 0$), is $u_M = A\lambda^2/4$, and the minimum velocity, achieved at the no-slip pipe walls ($y = \pm\lambda/2$), is $u_m = 0$.

The main assumption of the proposed model is the existence of the *porelet*. By porelet we mean the unit flow configuration at the pore scale (in our case, Poiseuille flow) that repeats itself, appropriately scaled, throughout the medium. Once the velocity fields have been simulated, we verify this central assumption by interpolating the modulus of the Eulerian velocity field along each pore throat (the segments of the Delaunay triangulation connecting disk walls) and fitting a parabola to the velocity profile from the high-resolution simulations. In Fig. 3 we show the magnitude of the velocity field along for four representative areas of the geometries studied and its profile projected along the four pore throats. The results illustrate that the velocity profile is well approximated by a parabola, thereby confirming our working hypothesis of a Poiseuille unit velocity configuration. We confirm this observation with a quantitative analysis over all pore throats in the five flow geometries studied. In each geometry, we compute the mean normalized residual $\langle r_u \rangle$ between the simulated profile and the parabolic fit (Table I). The mean residual is below 6.5% in all cases, demonstrating that assumption of Poiseuille flow at the pore throats is accurate.

The velocity PDF corresponding to each of these parabolic profiles is:

$$f_p(u) = -\frac{2}{\lambda}\frac{dy}{du} = \frac{2}{A\lambda^2\sqrt{1-\frac{4u}{A\lambda^2}}}. \tag{6}$$

For a collection of pipes with a given width distribution $f_\lambda(\lambda)$, Eq. (6) represents the conditional probability of the local velocity u $f_u(u|\lambda)$ within a pipe of given width λ. In our conceptual model, the overall flow consists of a randomly distributed collection of pore flow, the *porelet*, each of width λ (Fig. 2b). To obtain the equivalent of the Eulerian velocity PDF, we must integrate the PDF of all the porelets by weighing the contribution from each individual porelet by the length over which the parabolic profile applies. We conjecture, based on the direct numerical simulations at the pore scale, that such a length l is proportional to λ. Therefore, we recover the following scaling for our velocity distribution, controlled by an ensemble of porelets:

$$f_u(u) \sim \int_{\lambda_m(u)}^{\lambda_M} f_u(u|\lambda) f_\lambda(\lambda)\lambda \, d\lambda, \tag{7}$$

where $\lambda_m(u)$ is the pipe width such that the centerline velocity $u_M(\lambda) = u$, that is, $\lambda_m(u) = 2\sqrt{u/A}$, and λ_M is the maximum width of the distribution $f_\lambda(\lambda)$. Since we constructed our porous media such that the distribution of narrow throat widths scales as $f_\lambda(\lambda) \sim \lambda^{-\beta}$, we approximate Eq. (7) in the range of low velocities as

$$\begin{aligned} f_u(u) &\sim \int_{2\sqrt{u/A}}^{\lambda_M} \frac{2\lambda^{-\beta+1}}{A\lambda^2\sqrt{1-\frac{4u}{A\lambda^2}}}\, d\lambda \\ &\sim \frac{1}{2^\beta A}\left(\frac{u}{A}\right)^{-\beta/2} \int_{u/u_{\max}}^{1} x^{\frac{\beta}{2}-1}(1-x)^{-\frac{1}{2}}\, dx, \end{aligned} \tag{8}$$

where we introduced the change of variables $x = \frac{4u}{A\lambda^2}$, which plays the role of a rescaled velocity with respect to the centerline velocity of a pipe of width λ, $x = \frac{u}{u_M(\lambda)}$. In the range of low velocities, the limit of integration $u/u_{\max} \to 0$, and the definite integral in Eq. (8) converges to the Beta function $B\left(\frac{\beta}{2}, \frac{1}{2}\right)$ and loses its dependence on u. We conclude that our model of porelets for low velocities in a porous medium predicts a velocity distribution that scales as:

$$f_u(u) \sim u^{-\beta/2}. \tag{9}$$

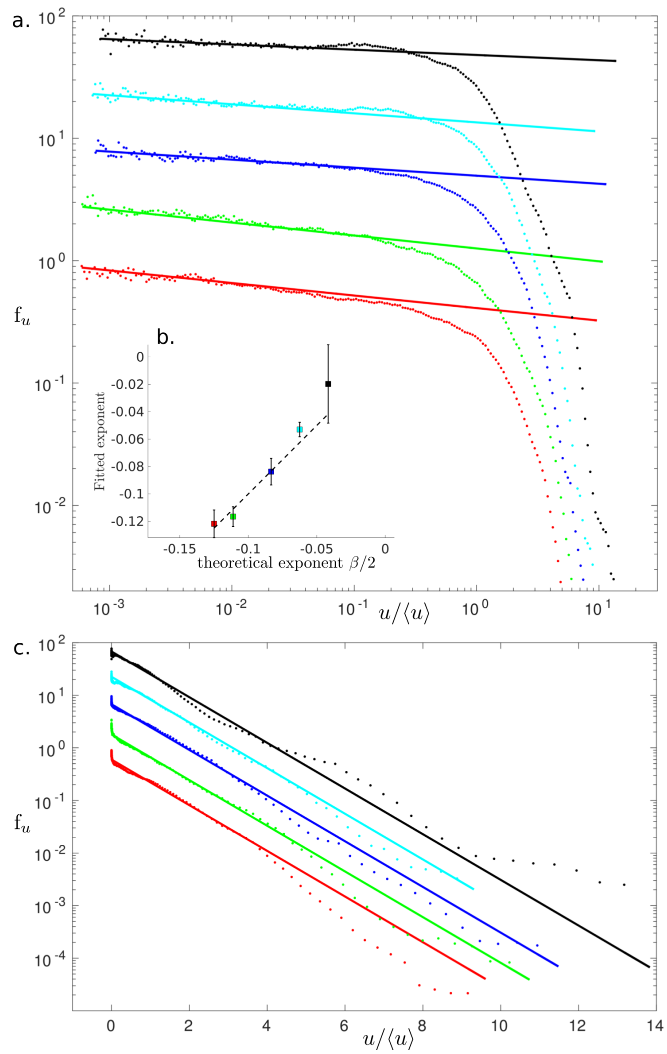

FIG. 4. a. PDF of the rescaled velocity magnitude, $u_r = u/\langle u \rangle$ for all five geometries studied, with $\beta = 0.25$ (red), $\beta = 0.22$ (green), $\beta = 0.17$ (blue), $\beta = 0.12$ (cyan), and $\beta = 0.083$ (black). Symbols correspond to the direct numerical simulations, and straight lines are the power-law fits to the symbols. Symbols and curves are shifted vertically for clarity. b. The fitted exponents plotted against the theoretical exponents $-\beta/2$ [Eq. (9)], where the error bars represent the standard deviation in the least-squares estimate of the time exponent. c. The symbols represent the same data as in a, but plotted in semi-logarithmic axes to highlight the exponential decay in the distribution of high velocities.

To test this prediction, we perform a power-law fit to the numerically simulated velocity distribution for each of the geometries considered (Fig. 4a), and we compare the fitted exponent with the theoretical exponent $-\beta/2$ (Fig. 4b).

We conclude that our simple conceptual model of a collection of porelets successfully captures the velocity distribution in the range of low velocities. The high velocities exhibit an exponential distribution that is largely insensitive to the statistical characteristics of the porous

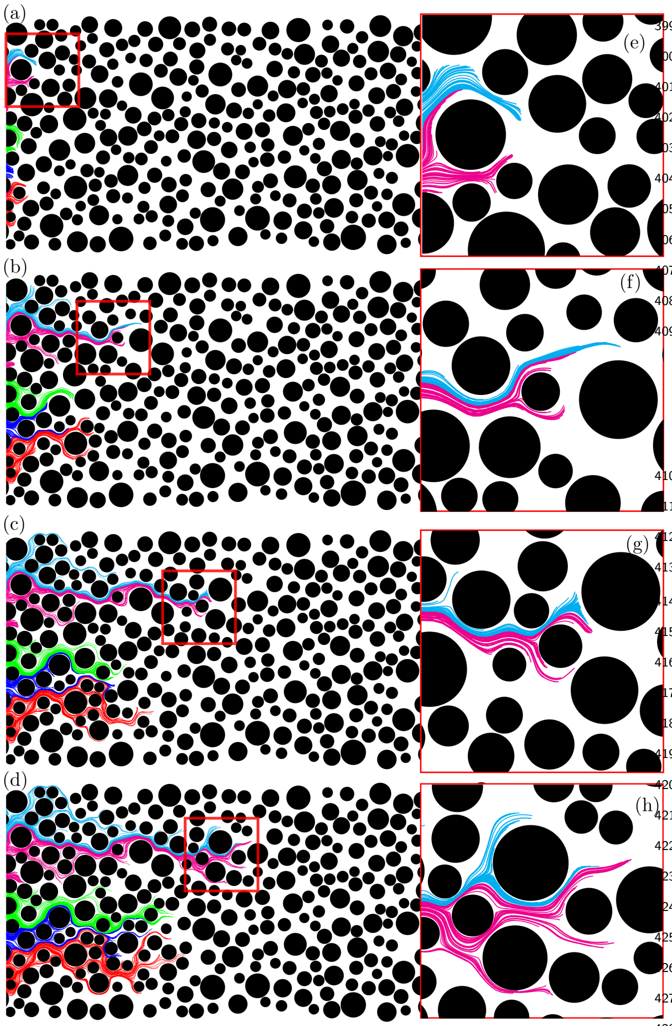

FIG. 5. Streamlines for 500 particles initialized at the left end of the channel at four equally spaced time steps. The different colors for different groups of particles help visualize the flow. On the right: magnification of small regions (the associated red boxes on the left), illustrating the quality of the streamlines furnished by our spectral-accurate velocity field and high-order time integrator.

medium geometry: the slope in Fig. 4c has value 1 for all geometries (the exponential distribution is parametrized by the average value only).

To illustrate the impact of fluid velocity heterogeneity and the importance of capturing the distribution of low velocities, we study macroscopic signatures of transport through the porous medium by tracking the displacement of fluid particles along streamlines (no diffusion, just advection). The fluid trajectories are computed using a fourth-order Runge–Kutta time stepping scheme. In the Runge–Kutta scheme, instead of evaluating the velocity $\boldsymbol{u}(\boldsymbol{x})$ using Eq. (2), we locally interpolate the fully resolved Eulerian grid near the particle location with a bicubic polynomial. Then the velocity at the particle location is approximated by evaluating the bicubic polynomial interpolant. By using the interpolant with a precomputed Eulerian grid rather than using Eq. (2), we greatly accelerate the streamline calculation. To illustrate the quality of the numerical solution, we plot the streamlines of 500 tracer particles initialized at the left end of the channel (Fig. 5), where same color identify groups of particle initiated within the same vertical segment at the left boundary.

At time t, the distance traveled by a particle j along its trajectory is $s_j(t)$. The first and second ensemble moments of s_j over the N_p simulated fluid particles are:

$$\langle s\rangle(t) = \frac{1}{N_p}\sum_{j=1}^{N_p} s_j(t), \quad \sigma_s^2(t) = \frac{1}{N_p}\sum_{j=1}^{N_p}\Big(s_j(t) - \langle s\rangle(t)\Big)^2. \tag{10}$$

In Fig. 6 we plot the temporal evolution of particle spreading $\sqrt{\sigma_s^2}$, as a function of time rescaled by the characteristic advective time across a pore, $\tau = \langle\lambda\rangle/\langle u\rangle$. Particle dispersion exhibits two power-law regimes $\sqrt{\sigma_s^2} \sim t^\alpha$. For $t/\tau < 1$, the fluid dispersion is ballistic ($\alpha = 1$), as expected since individual fluid particles have not yet explored enough space to significantly alter their velocity. For $t/\tau > 1$, the dispersion of fluid particles along their trajectories slows down, but it retains a super-diffusive behavior ($\alpha > 1/2$) which is persistent over two orders of magnitude in time. The transition time between these two regimes, $t/\tau \sim 1$, corresponds to the time when particles move between porelets, and therefore sample different velocities.

From the wide spectrum of statistical models of transport [e.g., 68–70], here we employ an uncorrelated Continuous Time Random Walk (CTRW) model that is known to reproduce late-time anomalous spreading from the broad velocity distribution [15], as we observe in our simulations. CTRW theory predicts the asymptotic scaling of tracer particle dispersion in Eq. (10) [15]:

$$\langle s\rangle(t) \sim t, \quad \sqrt{\sigma_s^2}(t) \sim t^{(1-\gamma)/2},$$

where γ is the characteristic exponent of the velocity distribution $\gamma = -\beta/2$, which leads to $\sqrt{\sigma^2} \sim t^{1/2+\beta/4}$, and is therefore super-diffusive for $\beta > 0$. The CTRW theory agrees well with the direct numerical simulations (Fig. 6). Therefore, the late-time scaling of tracer particle dispersion is controlled by the distribution of low velocities and, consequently, from the pore throat size distribution.

IV. CONCLUSION

In summary, we have taken steps to address a longstanding challenge in porous media flows: the relationship between pore structure and velocity distribution from Stokesian flow through the pore space. We have focused our study on describing the low velocities, as their distribution controls asymptotic properties of particle transport, fluid retention time, mixing efficiency, and reaction rates. We have proposed a conceptual model

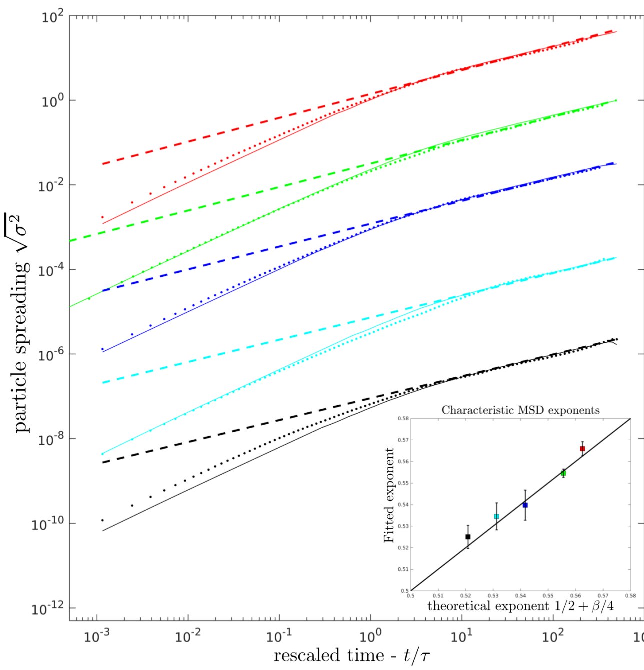

FIG. 6. Temporal evolution of particle spreading $\sqrt{\sigma_s^2}$ as a function of rescaled advective time, for the five geometries considered, with $\beta = 0.25$ (red), $\beta = 0.22$ (green), $\beta = 0.17$ (blue), $\beta = 0.12$ (cyan), and $\beta = 0.08$ (black). Symbols correspond to the results from direct numerical simulations. Dashed lines are power-law fits to the late-time spreading behavior, which show excellent agreement with the exponents predicted by CTRW theory with the velocity distribution from the proposed *porelet* model, $(t/\tau)^{(1/2+\beta/4)}$ (inset). Solid lines correspond to separate CTRW simulations that account for the correlation structure in the velocity field, which are capable of capturing the transition from the ballistic regime to the super-diffusive regime [19, 41].

of flow as a collection of *porelets*—here Hagen–Poiseuille parabolic flows through the throats width—from which we derive the scaling properties of the velocity distribution. Despite its simplicity, the analytical predictions from the model agree well with high-resolution simulations, both in terms of velocity distribution and the consequent anomalous particle spreading. Our results show that, for the cases studied, knowledge of the throat size distribution is sufficient to describe the PDF of low velocities (and, thus, the asymptotic transport properties), and that information about medium connectivity is not needed. This theoretical and computational study uncovers the analytical relationship between the pore throat size distribution and the distribution of fluid velocity. This conceptual model of porelets allows us to make predictions also for the statistics of fluid particles spreading along their own trajectories, which are confirmed by high fidelity simulations of Stokes flow and advective transport. While we have studied simple 2D porous media, the proposed framework is rather general, and the ability to work out the analytical predictions carries over to other flow configurations for which it is possible to disassemble the considered complex flow into a collection of known spatial velocity distributions. Indeed, we have recently started to extend our approach to simple but fully 3D geometries consisting of dense packs of polydisperse spherical beads [71], with encouraging results for the prediction of the entire velocity distribution from characteristics of the pore geometry. We plan to document these findings in a future manuscript.

ACKNOWLEDGMENTS

This work was funded by the US Department of Energy through 'DiaMonD', a DOE Mathematical Multifaceted Integrated Capability Center (grant DE-SC0009286).

[1] Y. E. Kutsovsky, L. E. Scriven, H. T. Davis, and B. E. Hammer, "NMR imaging of velocity profiles and velocity distributions in bead packs," Phys. Fluids **8**, 863–871 (1996).

[2] R. A. Freeze and J. A. Cherry, *Groundwater* (Prentice Hall, 1979).

[3] A. Boisson, P. de Anna, O. Bour, T. Le Borgne, T. Labasque, and L. Aquilina, "Reaction chain modeling of denitrification reactions during a push-pull test," J. Contaminant Hydrol. **148**, 1–11 (2013).

[4] L. Cueto-Felgueroso and R. Juanes, "Nonlocal interface dynamics and pattern formation in gravity-driven unsaturated flow through porous media," Phys. Rev. Lett. **101**, 244504 (2008).

[5] M. L. Szulczewski, C. W. MacMinn, H. J. Herzog, and R. Juanes, "Lifetime of carbon capture and storage as a climate-change mitigation technology," Proc. Natl. Acad. Sci. **109**, 5185 (2012).

[6] F. M. Orr, Jr. and J. J. Taber, "Use of carbon dioxide in enhanced oil recovery," Science **224**, 563–569 (1984).

[7] D. Wu, H. Liu, M. Xie, H. Liu, and W. Sun, "Experimental investigation on low velocity filtration combustion in porous packed bed using gaseous and liquid fuels," Exp. Ther. Fluid Sci. **36**, 169–177 (2012).

[8] C. Y. Wang, "Fundamental models for fuel cell engineering," Chem. Rev. **104**, 4727–4766 (2004).

[9] J. Bear, *Dynamics of Fluids in Porous Media* (Elsevier, New York, 1972).

[10] J. Kozeny, "Uber kapillare leitung der wasser in boden," Sitzungsber. Akad. Wiss. Wien **136**, 271–306 (1927).

[11] P. C. Carman, "Fluid flow through granular beds," Trans. Inst. Chem. Eng. **15**, 150–166 (1937).

[12] F. A. L. Dullien, *Porous Media: Fluid Transport and Pore Structure*, 2nd ed. (Academic Press, San Diego, Calif., 1991).

[13] O. Dardis and J. McCloskey, "Permeability porosity relationships from numerical simulations of fluid flow," Geophys. Res. Lett. **25** (1998).

[14] C. Chen, A. I. Packman, and G. F. gaillard, "Pore-scale analysis of permeability reduction resulting from colloid deposition," Geophys. Res. Lett. **35** (2008).

[15] M Dentz, A Cortis, H Scher, and B Berkowitz, "Time behavior of solute transport in heterogeneous media: transition from anomalous to normal transport," Adv. Water Resour. **27**, 155–173 (2004).

[16] D. Zhang and Q. kang, "Pore scale simulation of solute transport in fractured porous media," Geophys. Res. Lett. **31** (2004).

[17] T. Le Borgne, M. Dentz, and J. Carrera, "Lagrangian statistical model for transport in highly heterogeneous velocity fields," Phys. Rev. Lett. **101**, 090601 (2008).

[18] D. W. Meyer and H. A. Tchelepi, "Particle-based transport model with Markovian velocity processes for tracer dispersion in highly heterogeneous porous media," Water Resour. Res. **46**, W11552 (2010).

[19] P. K. Kang, P. de Anna, J. P. Nunes, B. Bijeljic, M. J. Blunt, and R. Juanes, "Pore-scale intermittent velocity structure underpinning anomalous transport through 3-D porous media," Geophys. Res. Lett. **41**, 6184–6190, doi:10.1002/2014GL061475 (2014).

[20] P. K. Kang, T. Le Borgne, M. Dentz, O. Bour, and R. Juanes, "Impact of velocity correlation and distribution on transport in fractured media: field evidence and theoretical model," Water Resour. Res. **51**, 940–959 (2015).

[21] B. Jha, L. Cueto-Felgueroso, and R. Juanes, "Fluid mixing from viscous fingering," Phys. Rev. Lett. **106**, 194502, doi:10.1103/PhysRevLett.106.194502 (2011).

[22] T. Le Borgne, M. Dentz, P. Davy, D. Bolster, J. Carrera, J. R. de Dreuzy, and O. Bour, "Persistence of incomplete mixing: A key to anomalous transport," Phys. Rev. E **84**, 015301 (2011).

[23] T. Le Borgne, M. Dentz, and E. Villermaux, "Stretching, coalescence and mixing in porous media," Phys. Rev. Lett. **110**, 204501 (2013).

[24] T. Le Borgne, M. Dentz, and E. Villermaux, "The lamellar description of mixing in porous media," J. Fluid Mech. **770**, 458–498 (2014).

[25] T. Tél, A. de Moura, C. Grebogi, and G. Károlyi, "Chemical and biological activity in open flows: A dynamical system approach," Phys. Rep. **413**, 91–196 (2005).

[26] T. W. Willingham, C. J. Werth, and A. J. Valocchi, "Evaluation of the effects of porous media structure on mixing-controlled reactions using pore-scale modeling and micromodel experiments," Environ. Sci. Technol. **42**, 3185 (2008).

[27] M. Dentz, T. Le Borgne, A. Englert, and B. Bijeljic, "Mixing, spreading and reaction in heterogeneous media: a brief review," J. Contaminant Hydrol. **120-121**, 1–17 (2011).

[28] P. de Anna, M. Dentz, A.M. Tartakovsky, and T. Le Borgne, "The filamentary structure of mixing fronts and its control on reaction kinetics in porous media flows," Geophys. Res. Lett. **41**, 4586–4593 (2014).

[29] P. de Anna, J. Jimenez-Martinez, H. Tabuteau, R. Turuban, T. Le Borgne, M. Derrien, and Y. Méheust, "Mixing and reaction kinetics in porous media: An experimental pore scale quantification," Env. Sci. Technol. **48**, 508–516 (2014).

[30] W.M. Durham, E. Climent, and R. Stocker, "Gyrotaxis in a steady vortical flow," Phys. Rev. Lett. **106**, 238102 (2011).

[31] F. Höfling and T. Franosch, "Anomalous transport in the crowded world of biological cells," Rep. Prog. Phys. **76**, 046602 (2013).

[32] L. Lebon, L. Oger, J. Leblond, J. P. Hulin, N. S. Martys, and L. M. Schwartz, "Pulsed gradient NMR measurements and numerical simulation of flow velocity distribution in sphere packings," Phys. Fluids **8**, 293–301 (1996).

[33] B. Manz, L. F. Gladden, and P. B. Warren, "Flow and dispersion in porous media: Lattice-Boltzmann and NMR studies," AIChE Journal **45**, 1845–1854 (1999).

[34] D. Kandhai, D. Hlushkou, A. G. Hoekstra, P. M. A. Sloot, H. VanAs, and U. Tallarek, "Influence of stagnant zones on transient and asymptotic dispersion in macroscopically homogeneous porous media," Phys. Rev. Lett. **88**, 234501 (2002).

[35] S. S. Datta, H. Chiang, T. S. Ramakrishnan, and D. A. Weitz, "Spatial fluctuations of fluid velocities in flow through a three-dimensional porous medium," Phys. Rev. Lett. **111**, 064501 (2013).

[36] M. Holzner, V. L. Morales, M. Willmann, and M. Dentz, "Intermittent Lagrangian velocities and accelerations in three-dimensional porous medium flow," Phys. Rev. E **92**, 013015 (2015).

[37] M. Levy and B. Berkowitz, "Measurement and analysis of non-Fickian dispersion in heterogeneous porous media," J. Contaminant Hydrol. **64**, 203 (2003).

[38] U. M. Scheven, D. Verganelakis, R. Harris, M. L. Johns, and L. F. Gladden, "Quantitative nuclear magnetic resonance measurements of preasymptotic dispersion in flow through porous media," Phys. Fluids **17**, 117107 (2005).

[39] B. Bijeljic, P. Mostaghimi, and M. J. Blunt, "Signature of non-Fickian solute transport in complex heterogeneous porous media," Phys. Rev. Lett. **107**, 204502 (2011).

[40] M. J. Blunt *et al.*, "Pore-scale imaging and modelling," Adv. Water Resour. **51**, 97–216 (2013).

[41] P. de Anna, T. Le Borgne, M. Dentz, A. Tartakovsky, D. Bolster, and P. Davy, "Flow intermittency, dispersion and correlated continuous time random walks in porous media," Phys. Rev. Lett. **101**, 184502 (2013).

[42] M. Icardi, G. Boccardo, D. L. Marchisio, T. Tosco, and R. Sethi, "Pore-scale simulation of fluid flow and solute dispersion in three-dimensional porous media," Phys. Rev. E **90**, 013032 (2014).

[43] F. Zami-Pierre, R. Loubens, M. Quintard, and Y Davit, "Transition in the flow of power-law fluids through isotropic porous media," Phys. Rev. Lett. **117** (2016).

[44] J. S. Andrade, Jr., M. P. Almeida, J. M. MendesFilho, S. Havlin, B. Suki, and H. E. Stanley, "Fluid flow through porous media: the role of stagnant zones," Phys. Rev. Lett. **79**, 3901–3904 (1997).

[45] M. Matyka, J. Gołembiewski, and Z. Koza, "Power-exponential velocity distributions in disordered porous media," Phys. Rev. E **93**, 013110 (2016).

[46] M. Siena, M. Riva, J. D. Hyman, C. L. Winter, and A. Guadagnini, "Relationship between pore size and velocity probability distributions in stochastically generated porous media," Phys. Rev. E **89**, 013018 (2014).

[47] M. Dentz, P. K. Kang, A. Comolli, T. Le Borgne, and D. R. Lester, "Continuous time random walks for the evolution of Lagrangian velocities," Phys. Rev. Fluids **1**, 074004 (2016).

[48] M. G. Trefry, F. P. Ruan, and D. McLaughlin, "Numerical simulations of preasymptotic transport in heterogeneous porous media: Departures from the Gaussian limit," Water Resour. Res. **39**, 1063 (2003).

[49] T. Le Borgne, M. Dentz, D. Bolster, J. Carrera, J.-R. de Dreuzy, and P. Davy, "Non-Fickian mixing: Temporal evolution of the scalar dissipation rate in heterogeneous porous media," Adv. Water Resour. **33**, 1468–1475 (2010).

[50] T. Le Borgne, and P. Gouze, "Non-Fickian dispersion in porous media: 2. Model validation from measurements at different scales," Water Resour. Res. **44**, W06427 (2008).

[51] A. Tyukhova, M Dentz, W. Kinzelbach, and M. Willmann, "Mechanisms of anomalous dispersion in flow through heterogeneous porous media," Phys. Rev. Fluids **1**, 074002(2016).

[52] J. R. Shewchuk, "Delaunay refinement algorithms for triangular mesh generation," Comput. Geom. **22**, 21–74 (2002).

[53] Q. Xiong, T. G. Baychev, and A. P. Jivkov, "Review of pore network modelling of porous media: Experimental characterisations, network constructions and applications to reactive transport," J. of Contam. Hydrol. **192**, 101–117 (2016).

[54] C. Pozrikidis, *Boundary Integral and Singularity Methods for Linearized Viscous Flow* (Cambridge University Press, New York, NY, USA, 1992).

[55] Lloyd N. Trefethen and J. A. C. Weideman, "The Exponentially Convergent Trapezoidal Rule," SIAM Review **56**, 385–458 (2014).

[56] Y. Saad and M.H. Schultz, "GMRES: A Generalized Minimal Residual Algorithm for Solving Nonsymmetric Linear Systems," SIAM Journal on Scientific and Statistical Computing **7**, 856–869 (1986).

[57] S. L. Campbell, I. C. F. Ipsen, C. T. Kelley, C. D. Meyer, and Z. Q. Xue, "Convergence estimates for solution of integral equations with gmres," Journal of Integral Equations and Applications **8**, 19–34 (1996).

[58] L. Greengard and V. Rokhlin, "A fast algorithm for particle simulations," J. Comput. Phys. **73**, 325–348 (1987).

[59] B. Quaife and G. Biros, "High-volume fraction simulations of two-dimensional vesicle suspensions," Journal of Computational Physics **274**, 245–267 (2014).

[60] I. Fatt, "The network model of porous media I. Capillary pressure characteristics," *Petrol. Trans.* AIME **207**, 144–159 (1956).

[61] I. Fatt, "The network model of porous media II. Dynamic properties of a single size tube network," *Petrol. Trans.* AIME **207**, 160–163 (1956).

[62] I. Fatt, "The network model of porous media III. Dynamic properties of networks with tube radius distribution," *Petrol. Trans.* AIME **207**, 164–181 (1956).

[63] M. Blunt and P. King, "Macroscopic parameters from simulations of pore scale flow," Phys. Rev. A **42**, 4780–4787 (1990).

[64] S. Bryant, P. R. King, and D. W. Mellor, "Network model evaluation of permeability and spatial correlation in a real random sphere packing," Transp. Porous Media **11**, 53–70 (1993).

[65] K. E. Thompson and H. S. Fogler, "Modeling flow in disordered packed beds from pore-scale fluid mechanics," AIChE J. **43**, 1337–1389 (1997).

[66] M. J. Blunt, "Flow in porous media—pore network models and multiphase flow," Curr. Opin. Colloid Interface Sci. **6**, 197–207 (2001).

[67] J. Happel and H. Brenner, *Low Reynolds Number Hydrodynamics* (Martinus Nijhoff Publishers, 1983).

[68] J. P. Bouchaud and A. Georges, "Anomalous diffusion in disordered media — Statistical mechanisms, models and physical applications," Phys. Rep. **195**, 127–293 (1990).

[69] R. Metzler and J. Klafter, "The random walks guide to anomalous diffusion: a fractional dynamics approach," Phys. Rep. **339**, 1–77 (2000).

[70] M. Dentz, D. R. Lester, T. Le Borgne, and F. P. J. de Barros, "Coupled continuous-time random walks for fluid stretching in two-dimensional heterogeneous media," Phys. Rev. E **94**, 061102 (2016).

[71] M. S. Kh. F. Sh. AlAdwani, *Prediction of Velocity Distribution from the Statistics of Pore Structure in 3D Porous Media via High-Fidelity Pore-Scale Simulation* (SM Thesis, Massachusetts Institute of Technology, 2017).

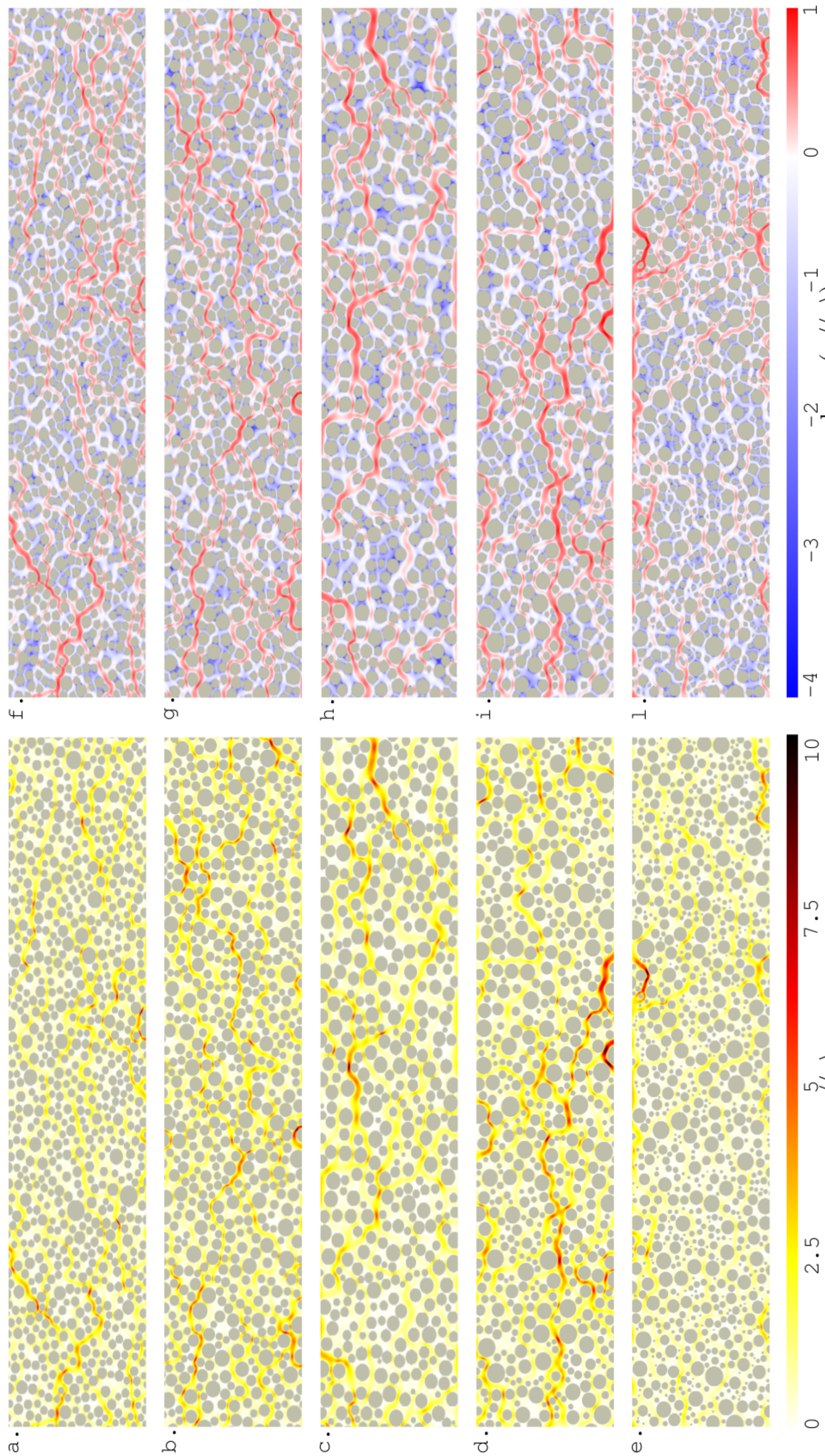

FIG. 7. The modulus of the rescaled velocity field $u/\langle u\rangle$ in each of the 5 considered geometries. On the left the color scale varies linearly, while on the right it changes logarithmically, showing the separation of the flow in channels of high velocity (red areas) and zones of stagnation (blue). The white color is associated to the average velocity.